JOURNAL OF THERMOPHYSICS AND HEAT TRANSFER
Vol. 14, No. 1, January–March 2000

Computational Study of Vibrationally Relaxing Gas past Blunt Body in Hypersonic Flows

Eswar Josyula*
U.S. Air Force Research Laboratory, Wright–Patterson Air Force Base, Ohio 45433-7913

Numerical simulations are presented of a steady-state, hypersonic flow over a two-dimensional cylinder of 1 m radius under conditions where the relaxation of the vibrational modes is significant. A Mach 6.5 nitrogen flow was simulated at freestream pressures of 50, 250, and 500 Pa, with a freestream translational temperature of 300 K. Two different freestream vibrational temperatures, 300 K (causing vibrational heating) and 4000 K (causing vibrational cooling) were considered to study the effects on the flowfield. An upwind-difference numerical scheme was used to solve the inviscid Euler equations coupled to the vibrational kinetic models of diatomic nitrogen, assumed as an anharmonic oscillator of 40 quantum levels using two sets of reaction rates. Comparison with previously reported computations showed a maximum variation of 10% in translational and first-level vibrational temperature along the surface due to differences in numerical schemes and grid densities; variation caused by the two different reaction rate sets was less than 2%. The vibrational cooling case showed a 10% higher shock-standoff distance than the vibrational heating case. The population distribution for the cooling case was non-Boltzmann due to nonresonant energy exchanges in the postshock region, greater in the shoulder region than in the stagnation region. An increase in freestream pressure for the cooling case increased the shock-standoff distance and non-Boltzmann behavior in the postshock region and near the surface. There was, however, a larger equilibrium region in between, in the stagnation region.

Nomenclature

e	= total energy per unit mass
i, j	= species indices in quantum levels v, w
l	= number of vibrational levels
M_∞	= freestream Mach number
p	= pressure
r	= nose radius
T	= translational temperature
T_{v1}	= first-level vibrational temperature
$T v_\infty$	= vibrational temperature in freestream used to set partial densities corresponding to a Boltzmann distribution
$\boldsymbol{u}$	= velocity vector
v, w	= vibrational quantum numbers
x, y	= Cartesian coordinates
Δ	= thermal disequilibrium parameter
δ	= shock-standoff distance
$\bar{\bar{\delta}}$	= Kronecker delta function
θ, ϕ	= angular spacing, deg
ρ	= total density
ρ_v	= state density in the vth vibrational level
∞	= freestream conditions subscript

Introduction

THE presence of a strong bow shock wave in hypersonic flow past a blunt forebody causes considerable difficulties for accurate numerical simulation of the flowfield in the stagnation region. The shock wave converts the high kinetic energy of the oncoming flow into various internal energy modes, which relax slowly, leading to significant chemical and thermal nonequilibrium in the stagnation region. Molecular collisions in a gas change the translational, rotational, vibrational, and electronic energies of the collision partners. The probabilities or effective cross sections of these elementary processes differ significantly, giving rise to widely separate relaxation times for the internal modes. Thus, it becomes important to understand the rates of relaxation processes to predict the nonequilibrium behavior of these kinds of flows. Vibrational equilibration is a process with relaxation times between the very short times for translational/rotational equilibration and the longer times for chemical and ionization equilibration.

In the recent years a number of computational studies appeared in the literature for hypersonic reentry conditions where the system of equations included the vibrational master equations to calculate the population distributions considering the kinetics of the particle exchanges among the quantum states.[1–4] Studies on flow past blunt bodies in previous research considered the translational temperature behind the shock to be higher than the vibrational temperature causing the vibrational modes to be heated in the shock layer. In contrast, if the translational temperature immediately behind the shock front is less than the vibrational temperature, the energy transfer process is reversed. This fundamental difference causes the temperature behind the shock to have additional dependence on the initial conditions for a shock wave propagating in a nonequilibrium vibrationally excited gas.[5] The present work computes such a case of vibrational cooling in the shock layer for a blunt-body flow. The work, an extension of Ref. 1, considers accuracy issues for nonequilibrium flow past a two-dimensional cylinder using a vibrational kinetics model and investigates flows undergoing vibrational cooling in the postshock region. Conditions of Ref. 1 were for Mach 6.5 nitrogen flow past an infinite cylinder of radius 1 m for a shock temperature below 3000 K.

The accuracy of the Roe upwind-difference method[6,7] in capturing shock-standoff distance for a dissociating gas was demonstrated in Ref. 8. The present work implements the upwind method to compute the test case presented by Giordano et al.[1] The vibrational–vibrational (V–V) and vibrational–translational (V–T) reaction rates are modeled as given in Ref. 1. These results are also compared with solutions using rates from the Schwartz–Slawsky–Herzfeld (SSH) theory to quantify variation, if any, on the flow parameters due to different rate sets. Effect of the number of quantum levels 10, 30, and 40, considered on the solution using rates from Ref. 1, are presented as part of the numerical accuracy studies.

The effect of an upstream freestream condition such that the vibrational temperature in the postshock region is higher than the translational temperature is computed for the Mach 6.5 nitrogen

Presented as Paper 99-0866 at the AIAA 37th Aerospace Sciences Meeting, Reno, NV, 11–14 January 1999; received 25 January 1999; revision received 30 July 1999; accepted for publication 24 August 1999.

*Research Aerospace Engineer, Air Vehicles Directorate. Associate Fellow AIAA.

flow past the blunt body. Influence of freestream pressures of 50 and 250 Pa on the flow properties for the case of vibrational cooling is also investigated.

Analysis

The global conservation equations in mass-averaged velocity form are

$$\frac{\partial}{\partial t}(\rho_v) + \nabla \cdot (\rho_v \boldsymbol{u}) = \dot{\omega}_v, \qquad v = 0, 1, \ldots \tag{1}$$

$$\frac{\partial}{\partial t}(\rho \boldsymbol{u}) + \nabla \cdot (\rho \boldsymbol{u}\boldsymbol{u} - p\bar{\bar{\delta}}) = 0 \tag{2}$$

$$\frac{\partial}{\partial t}(\rho e) + \nabla \cdot \left[\rho\left(e + \frac{p}{\rho}\right)\boldsymbol{u}\right] = 0 \tag{3}$$

The conservation Eq. (1) is written for mass density in quantum level v. The source term $\dot{\omega}_v$ derived from the vibrational master equations is made up of the relevant energy exchange processes consisting of the V–T and V–V reaction mechanisms. The equations governing the V–T reactions responsible for the variation of the particles distributed in the vth vibrational level are

$$N_2(v) + N_2 \rightleftharpoons N_2(v') + N_2 \tag{4}$$

and the equations governing the V–V processes giving the reactions responsible for the variation of the particles distributed in the vth vibrational level are

$$N_2(v) + N_2(w) \rightleftharpoons N_2(v') + N_2(w') \tag{5}$$

The kinetics of the particle exchanges among the quantum states are simulated by the vibrational master equation. The population distributions were calculated by[9]

$$\dot{\omega}_v = \frac{1}{M}\left\{ \sum_{v'} [k_{VT}(v' \rightarrow v)\rho_{v'}\rho - k_{VT}(v \rightarrow v')\rho_v\rho] + \sum_{w,v',w'} [k_{VV}(v', w' \rightarrow v, w)\rho_{v'}\rho_{w'} - k_{VV}(v, w \rightarrow v', w')\rho_v\rho_w] \right\} \tag{6}$$

In Eq. (6), the present calculations assume only single quantum transitions. The V–T process where the molecule loses or gains a vibrational quantum is shown in this equation. The replenishing rate from v' to v for colliding molecules is according to the rate of transition $k_{VT}(v' \rightarrow v)$ and the depleting rate from $v \rightarrow v'$ by $k_{VT}(v \rightarrow v')$. On the other hand, the collision partner participating in the V–V reaction process by the vibrational quantum exchange between colliding molecules gives rise to two states given by v and w; the transition rate to v and w is given by $k_{VV}(v', w' \rightarrow v, w)$ and the reverse rate by $k_{VV}(v, w \rightarrow v', w')$. The replenishing and depleting rates for the V–T and V–V contain both forward and backward rates (see Ref. 1 for more details).

The present study uses the same reaction rate coefficients as in Ref. 1: 1) V–T forward rate coefficients calculated according to expressions proposed by Capitelli et al.[10] and Billing and Fisher[11] and 2) V–V forward rates by Doroshenko et al.[12] Backward rate coefficients were derived from equilibrium considerations.

Rates from the SSH theory[13,14] were also used for purposes of comparison. For these, the required vibrational probability of transition $P_\tau(1, 0)$ was derived from the V–T rates of Billing and Fisher.[11] Table 1 is a summary of the rates used for different cases in the present study. A set of three-dimensional, semiclassical trajectory calculations for nitrogen rates computed by Billing and Fisher are widely accepted[15] as the most reliable theoretical data available. Figure 1a shows the comparison of the V–T rates used in the present study with Billing and Fisher's[11] exact calculations at $v = 9, 20, 30,$ and 40. The V–T rates of Ref. 1 match Billing and Fisher's rates,[11] very closely. The rates from SSH theory are shown at $v = 9$ and 40. At lower quantum numbers, for example, $v = 9$, the agreement with Ref. 1 and Billing and Fisher's rates,[11] is very good. However, as noted by other researchers (see Ref. 15), at high collision velocities and/or vibrational quantum numbers for which V–V–T becomes large, the use of the SSH theory has no theoretical basis. There is a greater discrepancy of the SSH rates with the Billing and Fisher's[11] at the higher levels; as an example, the V–T rates from SSH theory at $v = 40$ are shown in Fig. 1a. Figure 1b shows the V–V rates from Ref. 1 and SSH theory in comparison with rates from Billing and Fisher's exact calculations[11] at a temperature of 1000 K. The behavior at the lower quantum numbers where the rates peak to a high value is typical at other temperatures, 200, 300, 500, and 2000 K (plots not shown). The rates predicted by the SSH theory are lower than the rates of Ref. 1 and Billing and Fisher's rates[11] at these lower quantum numbers; the rates of Ref. 1 are higher than those of Billing and Fisher.[11] At higher quantum numbers, the discrepancy in the rates of Ref. 1 and SSH increases when compared to Billing and Fisher's rates.[11]

Table 1 Details of flow conditions: Mach number 6.5, T_∞ = 300 K

Tv_∞, K	p_∞, Pa	Levels	Rates
300	500	10	Ref. 1 and SSH
300	50	10, 30, 40	Ref. 1 and SSH
4000	50	40	Ref. 1
4000	250	40	Ref. 1

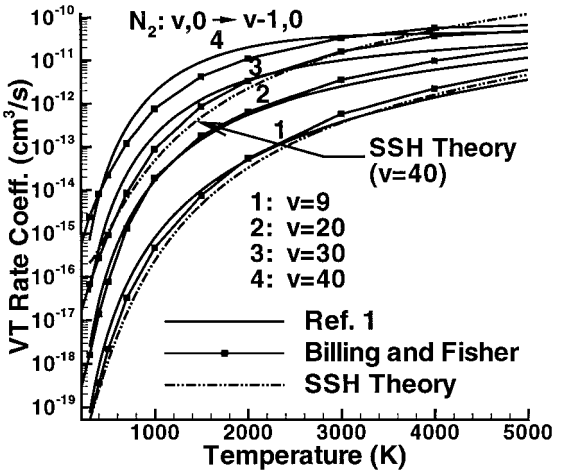

a) V–T rate coefficient

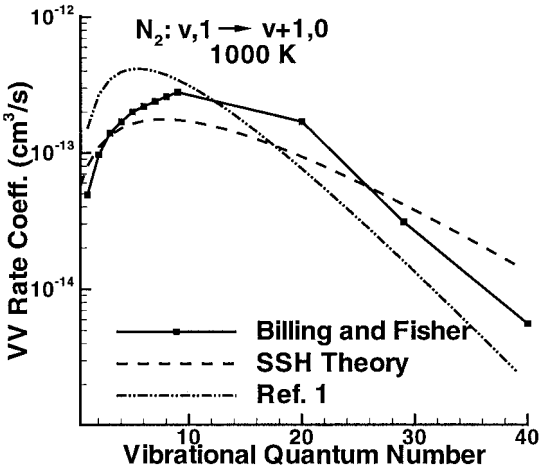

b) V–V Rate coefficient at 1000 K

Fig. 1 Rate coefficients used (Ref. 1 and SSH theory) compared with rates from Billing and Fisher's[11] exact calculations.

The vibrational energy is given in terms of the quantum level energies by

$$e_{\text{vib}} = \left(\frac{N_A}{M}\right) \sum_{i=1}^{l} \left(\frac{\rho_i}{\rho}\right) \epsilon_i \tag{7}$$

where the index i is used to denote the quantum level. In this equation, N_A is Avogadro's number, ρ_i/ρ is the fractional population of the ith vibrational level, M is the molecular weight, and ϵ_i is the quantum level energy given by the third-order approximating formula

$$\epsilon_i/hc = \omega_e(i - \tfrac{1}{2}) - \omega_e x_e(i - \tfrac{1}{2})^2 + \omega_e y_e(i - \tfrac{1}{2})^3$$
$$i = 1, 2, \ldots, l \tag{8}$$

Equation (8) represents anharmonic–oscillator behavior of the N_2 molecule, where h is Planck's constant and c is the speed of light. The spectroscopic constants are given by Ref. 16, $\omega_e = 2358.57$ cm^{-1}, $\omega_e x_e = 14.324$ cm^{-1}, and $\omega_e y_e = -0.00226$ cm^{-1}. When $i = 45$, the value of energy exceeds the N_2 dissociation energy, 9.62 eV (Ref. 17).

The first-level vibrational temperature T_{fl}, defined as the temperature corresponding to the Boltzmann distribution of the population ρ_1/ρ of the first vibrational level, is calculated by solving

$$\frac{\rho_1}{\rho} = \exp\left(\frac{-\epsilon_1}{kT_{\text{fl}}}\right) \Big/ \sum_{j=1}^{l} \exp\left(\frac{-\epsilon_j}{kT_{\text{fl}}}\right) \tag{9}$$

It may be noted that the T_{fl} is not very indicative of a vibrational temperature in the case of highly non-Boltzmann distributions.

Computations were performed to compare with results of Ref. 1 utilizing $l = 10$. Further computations for these conditions were made for $l = 30$ and 40 to study the effect of the number of levels considered on the solution. Remaining cases in this study were performed using $l = 40$. A summary of the cases is given in Table 1.

The numerical algorithm used to solve the coupled set of equations is the Roe flux difference method.[6] The method is implemented in finite volume formulation by computing the cell interface flux as described by Walters et al.[7] Second-order spatial accuracy is obtained by employing the MUSCL approach in conjunction with the minmod limiter to reduce the solution to first-order accuracy in the vicinity of strong shock waves, as described in the work of Josyula et al.[8] The entropy correction for the Roe scheme is implemented as discussed in Ref. 8. An explicit predictor–corrector method is used to advance the solution in time.

Convergence to a steady state solution was monitored by the L_2 norm. The data processing rate (DPR) for the two-dimensional solution of the Euler equations using the vibrational kinetics model with 40 quantum levels is 7.5×10^{-4} CPU seconds/grid point/iteration on a single processor of the Cray C-90 computer.

A grid size study was conducted to determine the effects of grid density on the temperature distribution along the stagnation streamline and surface. Details are given in Ref. 18. A mesh system of 40 nodes in the body-tangential direction and 50 nodes in the body-normal direction was used for all of the cases in the present study. The grid system for the two-dimensional cylinder is shown in Fig. 2. The minimum distance Δ_n/r of the first mesh point away from the body was 0.0012, and the grid was exponentially stretched in the body-normal direction with a stretch factor of 1.27.

The upstream and farfield boundary conditions are prescribed as the undisturbed freestream values. At the downstream boundary, the no-change condition is imposed for the predominantly supersonic flowfield. On the body surface, $\boldsymbol{n} \cdot \boldsymbol{u}$ is zero, where $\boldsymbol{n}$ is the surface normal vector. The finite volume formulation of the present work allows fluxes at the singular line of symmetry to be set to zero because the control surface of the elementary cell at the axis of symmetry merges to a point.

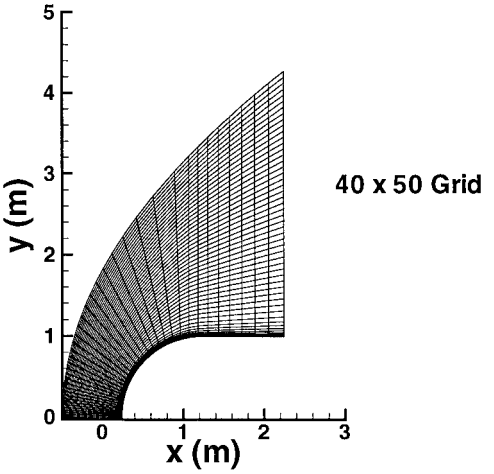

Fig. 2 Computational grid for two-dimensional cylinder.

The partial densities are set to values corresponding to a Boltzmann distribution at the temperature Tv_∞ on the first i levels of the spectrum produced by Eq. (8). Thus, $\rho_{i,\infty}$ is given by

$$\frac{\rho_{i,\infty}}{\rho_\infty} = \exp\left(\frac{-\epsilon_i}{kTv}\right) \Big/ \sum_{j=1}^{l} \exp\left(\frac{-\epsilon_j}{kTv}\right), \qquad i = 1, \ldots, l \tag{10}$$

For the vibrational heating case $Tv = 300$ K, and for the vibrational cooling case $Tv = 4000$ K (see Table 1).

Initial conditions were set to freestream uniform flow conditions for the vibrational heating cases with lower vibrational temperature. Other cases were started from these converged solutions.

Results and Discussion

Results are shown in two sections. In the first section are comparisons of current computations with those of Ref. 1 with reaction rates from SSH theory (for $l = 10$) and Ref. 1 (for $l = 10$, 30, and 40). The case of the vibrational cooling, that is, specifying a high vibrational temperature in the freestream to study its effect on the pressure, temperature, and fractional state densities, in the flowfield, is considered in the second section.

A note on the locations used for plotting population distribution. Population distributions vs quantum level vibrational energies [Eq. (8)] are plotted along four select locations along the stagnation streamline and at a line normal to the cylinder wall near the shoulder. The four locations are stream, preshock, postshock, and stagnation point (or surface). The stream location is at $(x/r = 1.55)$, the preshock (at the shock edge) location at the grid point immediately before the jump in T and p to their highest value across the shock, and the postshock location is the point immediately behind the shock front in the shock layer.

Comparison with Other Computational Results

In this section computational results of the present study are compared with the results of Ref. 1.

Temperature Comparisons Along Stagnation Streamline and Surface

The flow conditions used for the calculations shown in Figs. 3–6 are those used in Ref. 1: $M_\infty = 6.5$, $p_\infty = 50$ and 500 Pa, and $T_\infty = 300$ K, for diatomic nitrogen flow past an infinite cylinder of 1 m radius. Figures 3–6 show computational results using rates of Ref. 1 and SSH theory. The results as seen in Figures 3–6 are representative of the differences in shock capturing by the two numerical schemes: 1) the central difference method used in Ref. 1 and 2) the Roe flux difference (upwind) method used in the present study.

Comparisons are shown of translational temperature T and first-level vibrational temperature T_{fl} along the stagnation streamline and along the surface for computations at $p_\infty = 500$ Pa (Figs. 3 and 4)

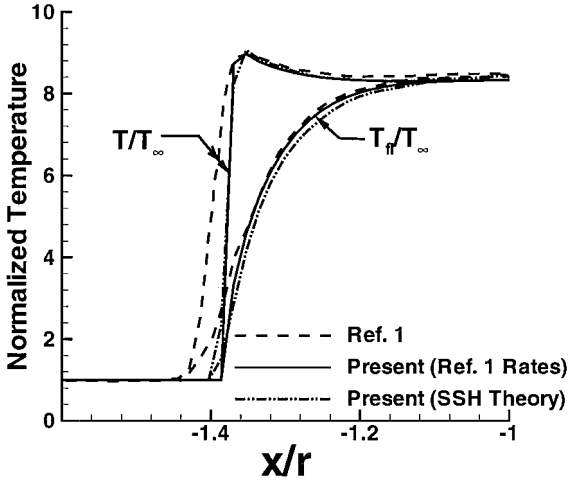

Fig. 3 Comparison of T and T_{fl} along stagnation streamline: $M_\infty = 6.5, p_\infty = 500$ Pa, $Tv_\infty = 300$ K, and $T_\infty = 300$ K.

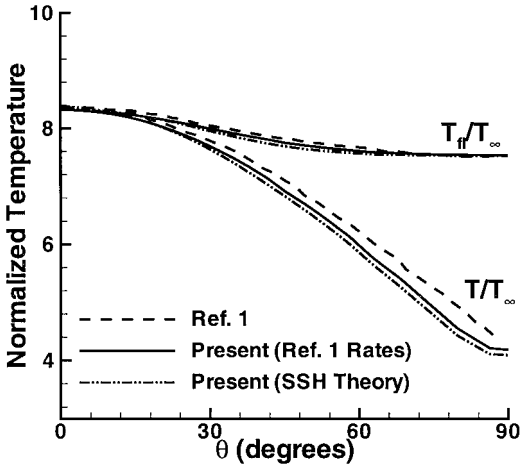

Fig. 4 Comparison of T and T_{fl} along surface: $M_\infty = 6.5, p_\infty = 500$ Pa, $Tv_\infty = 300$ K, and $T_\infty = 300$ K.

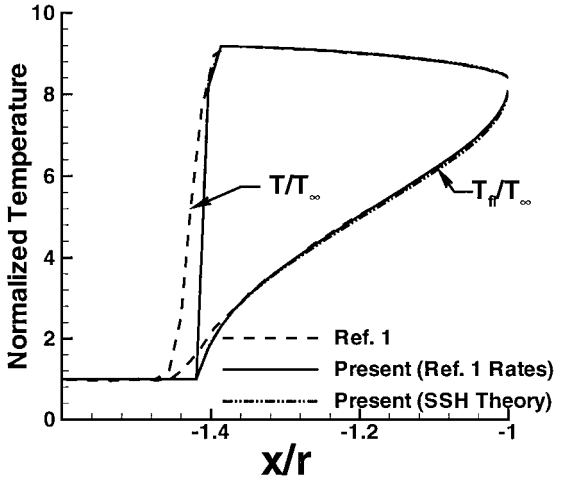

Fig. 5 Comparison of T and T_{fl} along stagnation streamline: $M_\infty = 6.5, p_\infty = 50$ Pa, $Tv_\infty = 300$ K, and $T_\infty = 300$ K.

and at $p_\infty = 50$ Pa (Figs. 5 and 6). The comparison along the stagnation streamline (Figs. 3 and 5) shows a greater smearing of the shock jump of Ref. 1. In the shock layer, however, the differences in temperatures between the two methods are very small. The first-level temperatures predicted in the present study, using the SSH rates along the stagnation streamline and surface, are consistently lower than those of Ref. 1 rates, a consequence of lower V–V rates at lower quantum numbers, shown earlier in Fig. 1b.

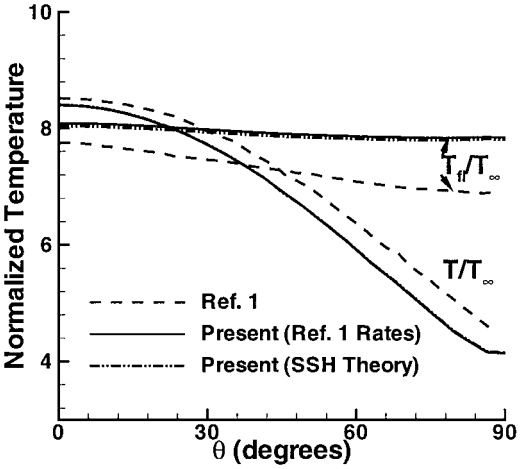

Fig. 6 Comparison of T and T_{fl} along surface: $M_\infty = 6.5, p_\infty = 50$ Pa, $Tv_\infty = 300$ K, and $T_\infty = 300$ K.

Along the surface for $p_\infty = 500$ Pa (Fig. 4), the translational temperature T predicted by the present study (Ref. 1 rates) is lower than that of Ref. 1 by 4%. Prediction of T by the present computation using the rates of Ref. 1 is higher than that of SSH rates by 2%. The variation between all three cases for the first level temperature T_{fl} at $p_\infty = 500$ Pa along the surface is small.

Along the surface for $p_\infty = 50$ Pa (Fig. 6), the translational temperature T predicted by the present study (Ref. 1 rates) is lower by 9% and the first-level temperature T_{fl} higher by 11% compared to the results shown in Ref. 1. The variations given are the maximum and are located at the shoulder of the blunt body. These can be attributed to the differences in grid density and numerical algorithms used in the studies. It is noted that the variation in prediction of temperatures due to differences in rates used, namely, Ref. 1 and SSH theory, is less than 1%. Rates from Ref. 1 were used to compute the rest of the cases in this study.

Effect of Number of Levels Considered on Population Distribution

The effect of the number of vibrational levels considered, $l = 10$, 30, and 40, on the energy level distribution is shown in Figs. 7a and 7b. Figures 7a and 7b show fractional state density vs vibrational quantum level energies with the corresponding quantum numbers also shown along the curves. At select locations (explained in the beginning of this section), the fractional state density is plotted in Fig. 7a along the stagnation streamline and in Fig. 7b along a line normal to the cylinder wall at the shoulder. From Figs. 7a and 7b, it is seen that the population distribution is Boltzmann in the freestream and becomes non-Boltzmann in the shock layer. Although non-Boltzmann, the fractional state density is too small to have any significant effect on the flow properties. At the edge of the shock location, marked in Figs. 7a and 7b as preshock, the population distribution for 30 levels is an extension of 10 levels, as expected. Note, however, that the computation considering 40 levels predicts a higher fractional state density after 7 levels in the stagnation region (Fig. 7a) and 13 levels in the shoulder region (Fig. 7b). The partitioning of energy into the higher levels for the 40-level computation alters the shock location slightly and, thereby, predicts the increased fractional state density; this increase is an indication of the accuracy of the computation and has negligible effect on the pressure and temperature. The remaining curves in Figs. 7a and 7b for $l = 10$, 30, and 40 lie on top of each other. The rest of the cases in this study were computed with $l = 40$.

Effect of Higher Vibrational Temperatures

The results in this section are discussed for flows with the conditions $M_\infty = 6.5$ and $T_\infty = 300$ K for a higher vibrational temperature than in the preceding cases. The effect of an increased vibrational temperature in the freestream given by $Tv_\infty = 4000$ K for $p_\infty = 50$ Pa is shown in Figs. 8–10. Unlike the preceding cases, here $Tv_\infty > T$ in the freestream and $T_{fl} > T$ behind the shock. This results in the vibrational modes giving up their energy to the translational

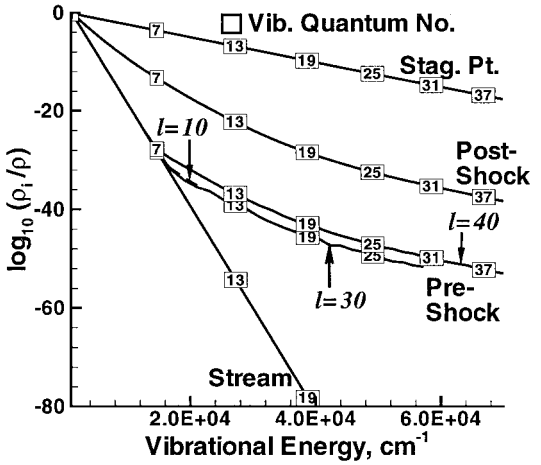

a) Along stagnation streamline

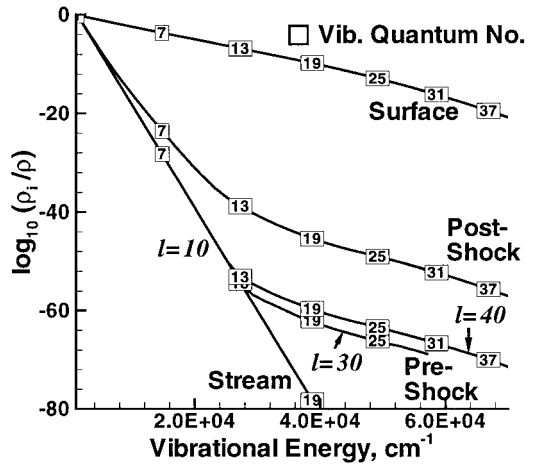

b) Normal to cylinder wall at shoulder

Fig. 7 For 10-, 30-, and 40-level population distribution: $M_\infty = 6.5$, $p_\infty = 50$ Pa, $Tv_\infty = 300$ K, and $T_\infty = 300$ K.

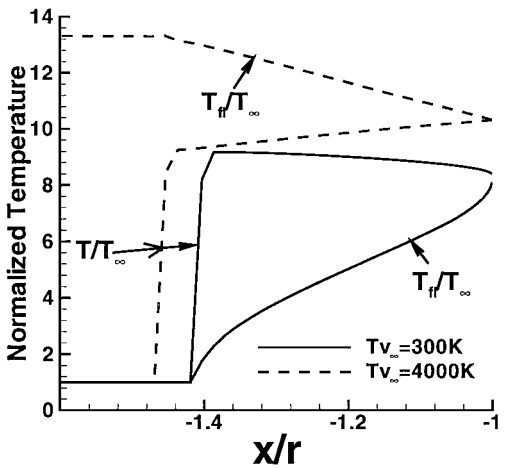

Fig. 8 Temperature distribution along stagnation streamline: $M_\infty = 6.5$, $p_\infty = 50$ Pa, $Tv_\infty = 300$ and 4000 K, and $T_\infty = 300$ K.

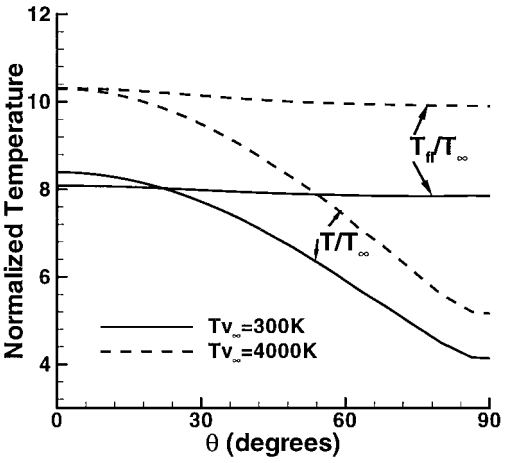

Fig. 9 Temperature distribution along surface: $M_\infty = 6.5$, $p_\infty = 50$ Pa, $Tv_\infty = 300$ and 4000 K, and $T_\infty = 300$ K.

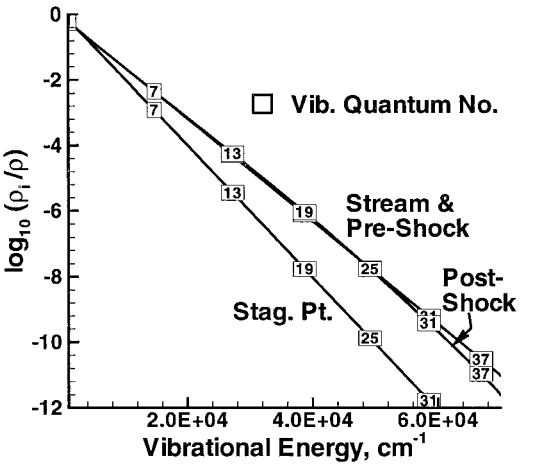

a) Along stagnation streamline

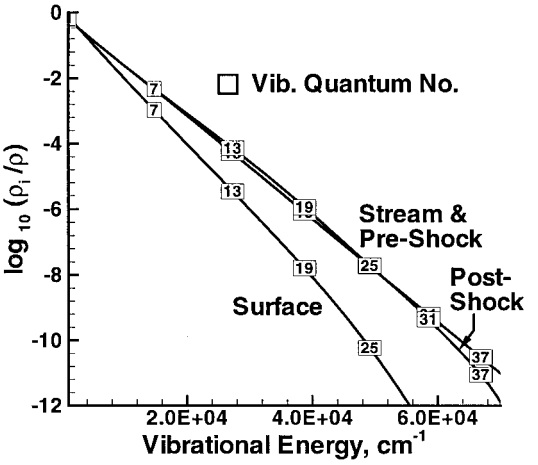

b) Normal to cylinder wall at shoulder

Fig. 10 Population distribution, $M_\infty = 6.5$, $p_\infty = 50$ Pa, $Tv_\infty = 4000$ K, and $T_\infty = 300$ K.

degree of freedom. Figures 8 and 9, showing temperature distributions, also show the results of the preceding case for comparison.

The temperatures (T and T_{fl}) along the stagnation streamline are shown in Fig. 8. The high first-level vibrational temperature (for $Tv_\infty = 4000$ K) stays nearly constant in the preshock region, then decreases in the shock layer. Correspondingly, the translational temperature jumps up across the shock and increases in the shock layer; the additional vibrational energy introduced before the shock undergoes V–V and V–T exchanges and causes the increase in the translational temperature. Both translational and vibrational temperatures equilibrate at the stagnation point. The shock-standoff distance increases for the case of $Tv_\infty = 4000$ K, compared to the $Tv_\infty = 300$ K case accompanied by a decrease in density in the shock layer (discussed later).

The temperatures (T and T_{fl}) along the surface are shown in Fig. 9. Because of the increase in Tv_∞, the increase in T at the stagnation point is 23% ($\theta = 0$ deg) and 25% at the shoulder ($\theta = 90$ deg). The T_{fl} increases by about 27% along the surface. It is noted that, unlike

the case of lower Tv_∞, the temperatures are in equilibrium at the stagnation point.

These effects can be seen in Fig. 10 with respect to the population distribution along the stagnation streamline and a line normal to the wall at the shoulder. Unlike the preceding cases, there is cooling of the vibrational levels across the shock layer and significantly higher fractional state densities in the upper quantum levels. The distributions are Boltzmann upstream of the shock and stagnation point locations. In the postshock location the situation is as follows. The lower level relaxation is dominated by V–V exchanges, and the upper levels increase in population by excitation of molecules in lower levels. The distribution undergoes V–V exchanges populating the upper levels at the expense of lower levels. Also, V–T losses take place in the higher energy levels, noticeable in Fig. 10 by the drop of the upper part of the tail causing the energy to cascade down to lower levels. The occurrence of V–V exchanges and V–T losses is seen as a bulge in the intermediate levels between 13 and 25 with higher fractional state densities. These effects are enhanced in the shoulder region (Fig. 10b), where the translational temperature drops from the temperature in the stagnation region (see Fig. 9). In the shoulder region, the population distribution near the surface also shows the tail dip beyond quantum number 25.

It is clear from the preceding discussion that a vibrational temperature higher than translational temperature behind the shock cools the vibrational modes, populates the higher energy levels, and causes non-Boltzmann distributions due to nonresonant energy transfer in the shock layer.

Effect of Higher Freestream Pressure

For the vibrational cooling case, results are discussed for an increase in the freestream pressure from $p_\infty = 50$ to 250 Pa (Figs. 11–13).

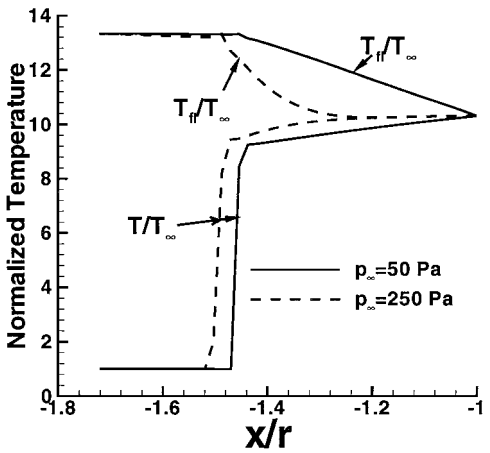

Fig. 11 Temperature distribution along stagnation streamline: M_∞ = 6.5, p_∞ = 50 and 250 Pa, Tv_∞ = 4000 K, and T_∞ = 300 K.

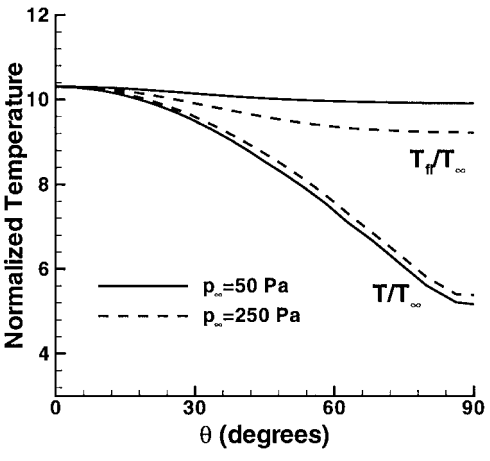

Fig. 12 Temperature distribution along surface: M_∞ = 6.5, p_∞ = 50 and 250 Pa, Tv_∞ = 4000 K, and T_∞ = 300 K.

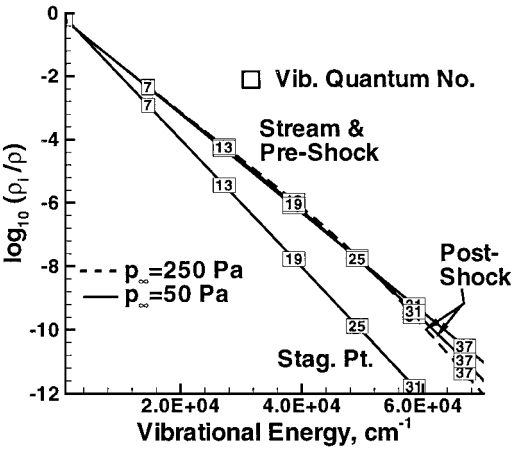

a) Along stagnation streamline

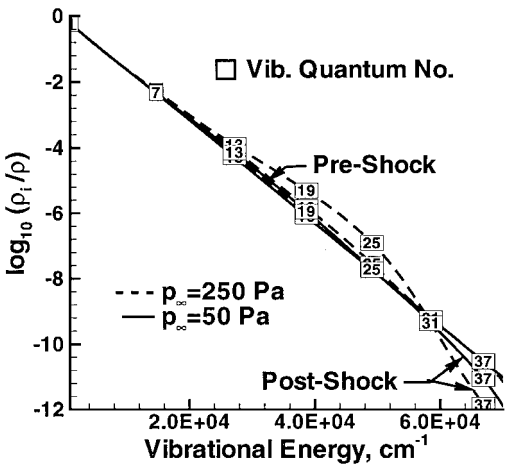

b) Normal to cylinder wall at shoulder (pre- and postshock)

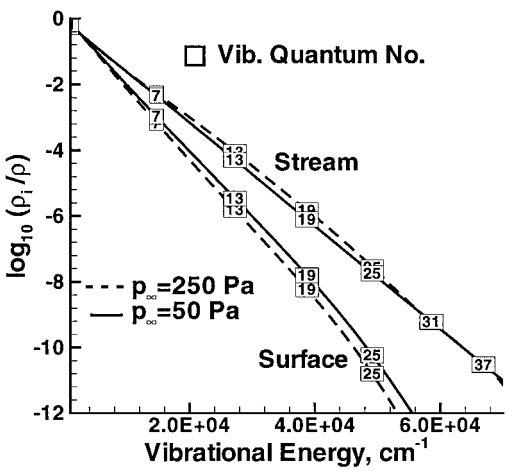

c) Normal to cylinder wall at shoulder (stream and surface)

Fig. 13 Population distribution: M_∞ = 6.5, p_∞ = 50 and 250 Pa, Tv_∞ = 4000 K, and T_∞ = 300 K.

The effects on the temperatures (T and T_{ff}) along the stagnation streamline are shown in Fig. 11. For the higher pressure case, the higher collision frequency and the shorter relaxation time cause the temperatures in the shock layer to equilibrate closer to the shock. This results in a higher translational temperature and a lower density (figure shown later) in the shock layer causing the shock-standoff distance to increase.

The changes in the temperatures (T and T_{ff}) along the surface in Fig. 12 show the effect of a more rapid V–T exchanges in a shortened relaxation time resulting in higher T and lower T_{ff} for the high-pressure case. The maximum variation caused by the higher pressure is 5% in translational temperatures and 7% in first-level vibrational temperatures.

These effects are also seen in the population distribution along the stagnation streamline and a line normal to the wall at the shoulder shown in Fig. 13. In the upstream region of the shock and at the stagnation point, the distribution is Boltzmann in the stagnation region (Fig. 13a). At the postshock location, the dip in the distribution at the higher levels due to V–T exchanges is higher for the high-pressure case. Correspondingly, there is an increase in fractional state density between quantum numbers 13 and 31. The non-Boltzmann behavior is further enhanced in the shoulder region (Fig. 13b).

The population distributions in freestream and surface locations of the shoulder region are shown for both pressures in Fig. 13c. Note that there is higher fractional state density between quantum numbers 7 and 31 in the stream location for the high-pressure case. Before the freestream flow encounters the shock, the higher pressure enhances the collison rate in the freestream, and the large difference in translational and vibrational temperatures causes variation in the population distribution. The lower fractional state density at the surface for the higher pressure case corresponds to the prediction of a lower T_{fi} near the surface seen earlier in Fig. 12.

Pressure and Density Distributions

The nondimensional pressure and density distributions along the stagnation streamline together with the shock-standoff distances for all cases considered are shown in Figs. 14–16. The magnitude of pressure jump across the shock is nearly the same for all cases (Fig. 14); the nondimensional pressure variation in the shock layer for all cases is also negligible. However, the shock-standoff distances show variation. For the cases having $Tv_\infty = 300$ K, the shock-standoff distance decreases by 8% for an increase in p_∞ from 50 Pa to 500 Pa. This trend is opposite to the cases with $Tv_\infty = 4000$ K, where the shock-standoff distance increases by about 10% for an increase in p_∞ from 50 to 250 Pa (also see Fig. 15).

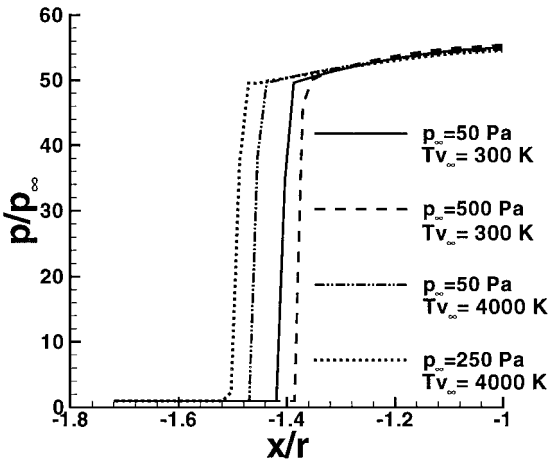

Fig. 14 Normalized-pressure distribution along stagnation streamline: $M_\infty = 6.5$ and $T_\infty = 300$ K.

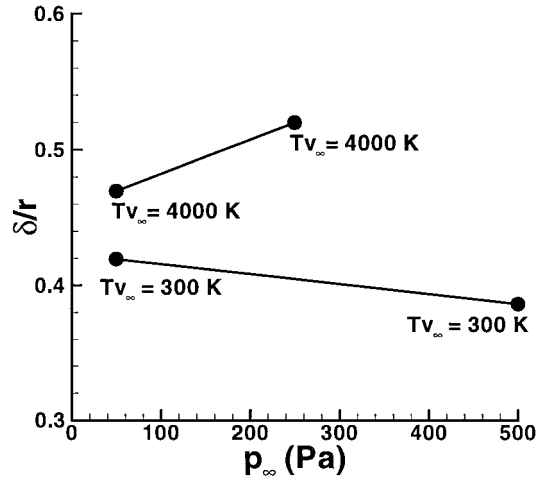

Fig. 15 Shock-standoff distance: $M_\infty = 6.5$ and $T_\infty = 300$ K.

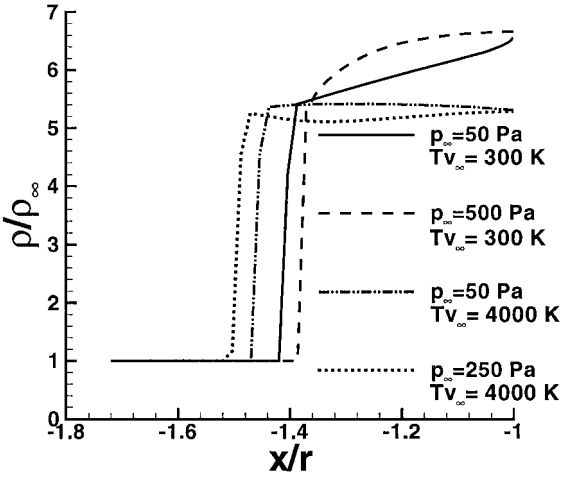

Fig. 16 Normalized-density distribution along stagnation streamline: $M_\infty = 6.5$ and $T_\infty = 300$ K.

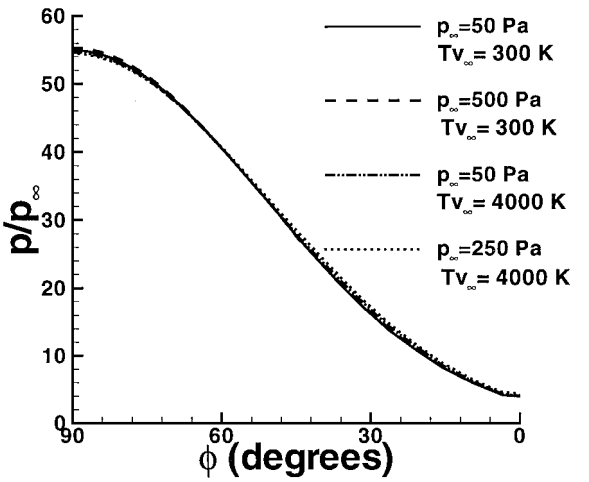

Fig. 17 Normalized-pressure distribution along surface: $M_\infty = 6.5$ and $T_\infty = 300$ K.

The changes in the shock standoff distance are accompanied by the changes in density inside the shock layer (Fig. 16). The density across the shock layer increases for the cases having $Tv_\infty = 300$ K and decreases for the cases of $Tv_\infty = 4000$ K. It is further noted that, at $p_\infty = 50$ Pa, increasing the Tv_∞ from 300 to 4000 K increases the shock-standoff distance by 10%.

The pressure distribution along the surface is shown in Fig. 17. The nondimensional pressure shows little variation for all of the cases considered in this study.

The thermal disequilibrium regions for the vibrational heating and cooling cases are shown by contour plots in Fig. 18; the thermal disequilibrium parameter is defined as[1]

$$\Delta = 100[(T - T_{fi})/T] \tag{11}$$

For the vibrational heating case (at lower Tv_∞), the region of $\Delta < 0$ (Fig. 18a) is confined to a small region beyond the shoulder of the cylinder, also seen in Ref. 1. For the vibrational cooling case (at higher Tv_∞) (Figs. 18b and 18c), the region of $\Delta < 0$ extends from the stagnation region to the downstream region. The higher pressure case (Fig. 18c) displays a larger nonequilibrium region near the shock and surface; however, in the stagnation region in between, there is a larger equilibrium region.

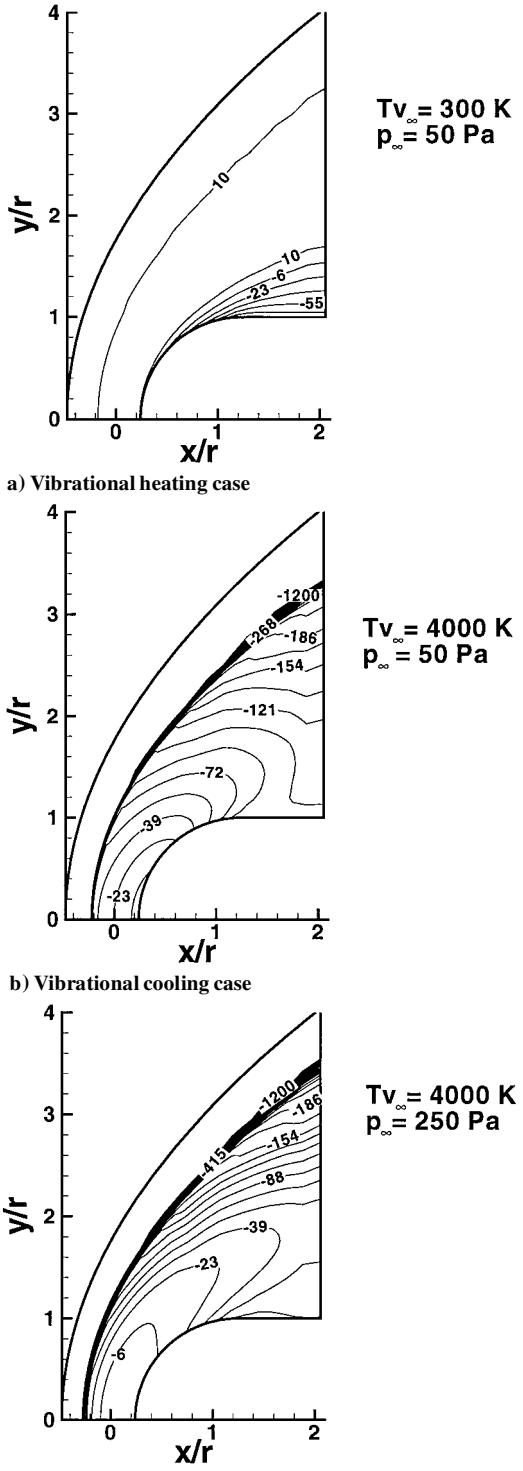

Fig. 18 Comparison of thermal disequilibrium regions: $M_\infty = 6.5$, $T_\infty = 300$ K, contours of $\Delta = 100[(T - T_{fl})/T]$.

Conclusion

A computational study was conducted of hypersonic flow past a two-dimensional cylinder. The flow conditions were Mach number 6.5 at p_∞ ranging from 50 to 500 Pa and $T_\infty = 300$ K for a 1-m-radius body. The inviscid Euler equations were coupled to the vibrational master equations with 40 quantum energy levels of diatomic nitrogen, assumed as an anharmonic oscillator. The master equations account for the V–T and V–V energy exchange processes. A vibrational heating case ($Tv_\infty = 300$ K) and a vibrational cooling case ($Tv_\infty = 4000$ K) were investigated to study effects on the flowfield.

Comparison of the results for the baseline vibrational heating case with a previous study showed a maximum difference of 10% in the predictions of the first-level vibrational temperatures along the surface due to differences in numerical methods and grid densities used. The difference in the temperature predictions in the shock layer between the two sets of reaction rates used in the present study is less than 2%.

The vibrational cooling case exhibited greater non-Boltzmann distributions due to non-resonant energy exchanges and higher population densities in the upper levels. The effect of strong V–T exchanges at the higher quantum numbers resulted in the lowering of the fractional state density beyond quantum number of 31 and an increase in intermediate levels, between quantum numbers of 7 and 31, away from the Boltzmann distribution. The non-Boltzmann behavior was stronger in the shoulder region of the blunt body. An increase of p_∞ from 50 to 250 Pa also contributed to a greater non-Boltzmann behavior behind the shock and near the surface; however, the nonequilibrium flow equilibrated closer to the shock in the stagnation region.

The nondimensional pressure jump across the shock was nearly the same for all cases, but the shock-standoff distance varied. The shock-standoff distance predicted by the vibrational cooling case was 10% higher than the vibrational heating case. A further increase in the standoff distance results when the freestream pressure is increased from 50 to 250 Pa. The increases in the shock-standoff distances were accompanied by lower densities in the shock layer.

Acknowledgments

This research was supported under Air Force Office of Scientific Research contracts monitored by M. Jacobs and S. Walker. The major part of computer resources were provided by the Department of Defense High Performance Computing Major Shared Resource Center at the Naval Oceanographic Office, Bay St. Louis, Mississippi. The author is thankful to C. DeJoseph (Air Force Research Laboratory) for helpful discussions and providing the computer code for the Schwartz–Slawsky–Herzfeld rate computation. Discussions with W. Bailey (Air Force Institute of Technology) and P. Cinnella (Mississippi State University) are gratefully acknowledged.

References

[1]Giordano, D., Bellucci, V., Colonna, G., Capitelli, M., Armenise, I., and Bruno, C., "Vibrationally Relaxing Flow of N_2 Past an Infinite Cylinder," *Journal of Thermophysics and Heat Transfer*, Vol. 11, No. 1, 1997, pp. 27–35.

[2]Candler, G. V., Olejniczak, J., and Harrold, B., "Detailed Simulation of Nitrogen Dissociation in Stagnation Region," *Physics of Fluids*, Vol. 9, No. 7, 1997, pp. 2108–2117.

[3]Armenise, I., Capitelli, M., Colonna, G., and Gorse, C., "Nonequilibrium Vibrational Kinetics in the Boundary Layer of Re-Entering Bodies," *Journal of Thermophysics and Heat Transfer*, Vol. 10, No. 3, 1996, pp. 397–405.

[4]Ruffin, S. M., "Prediction of Vibrational Relaxation in Hypersonic Expanding Flows Part II: Results," *Journal of Thermophysics and Heat Transfer*, Vol. 9, No. 3, 1995, p. 438.

[5]Osipov, A. I., and Uvarov, A. V., "Kinetic and Gasdynamic Processes in Nonequilibrium Molecular Physics." *Soviet Physics—Uspekhi*, Vol. 35, No. 11, 1992, pp. 903–923.

[6]Roe, P. L., "Approximate Riemann Solvers, Parameter Vectors and Difference Schemes," *Journal of Computational Physics*, Vol. 43, Oct. 1981, pp. 357–372.

[7]Walters, R. W., Cinnella, P., and Slack, D. C., "Characteristic-Based Algorithms for Flows in Thermochemical Nonequilibrium," *AIAA Journal*, Vol. 30, No. 5, 1992, pp. 1304–1313.

[8]Josyula, E., Gaitonde, D., and Shang, J. S., "Hypersonic Nonequilibrium Flow Computations Using the Roe Flux-Difference Split Scheme," *AIAA Journal*, Vol. 31, No. 5, 1993, pp. 812, 813.

[9]Adamovich, I. V., Macheret, S. O., Rich, J. W., and Treanor, C. E., "Vibrational Relaxation and Dissociation Behind Shock Waves, Part 2: Master Equation Modeling," *AIAA Journal*, Vol. 33, No. 6, 1995, pp. 1070–1075.

[10]Capitelli, M., Gorse, C., and Billing, G. D., "V-V Pumping Up in Nonequilibrium Nitrogen: Effects on the Dissociation Rate," *Chemical Physics*, Vol. 52, No. 3, 1980, pp. 299–304.

[11]Billing, G. D., and Fisher, E. R., "VV and VT Rate Coefficients in Diatomic Nitrogen by a Quantum Classical Model," *Chemical Physics*, Vol. 43, No. 3, 1979, pp. 395–401.

[12]Doroshenko, V. M., Kudryavtsev, N. N., Novikov, S. S., and Smetanin, V. V., "Effect of the Formation of Vibrationally Excited Nitrogen Molecules in Atomics Recombination in a Boundary Layer on the Heat Transfer," *High Temperature (USSR)*, Vol. 28, No. 1, 1990, pp. 82–89.

[13]Bray, K. N. C., "Vibrational Relaxation of Anharmonic Oscillator Molecules: Relaxation Under Isothermal Conditions," *Journal of Physics B*, Vol. 1, Series 2, 1968, pp. 705–717.

[14]Keck, J. C., and Carrier, G., "Diffusion Theory of Nonequilibrium Dissociation and Recombination," *Journal of Chemical Physics*, Vol. 43, No. 7, 1965, pp. 2284–2298.

[15]Adamovich, I. V., Macheret, S. O., Rich, J. W., and Treanor, C. E., "Vibrational Relaxation and Dissociation Behind Shock Waves, Part 1: Kinetic Rate Models," *AIAA Journal*, Vol. 33, No. 6, 1995, pp. 1064–1069.

[16]Huber, K. P., and Herzberg, G., *Constants of Diatomic Molecules*, Van Nostrand Reinhold Co., New York, 1979, pp. 420, 421.

[17]Armenise, I., Capiteill, M., Celiberto, R., Colonna, G., and Gorse, C., "The Effect of $N + N_2$ Collisions on the Non-Equilibrium Vibrational Distributions of Nitrogen Under Reentry Conditional," *Chemical Physics Letters*, Vol. 227, No. 1, 1994, pp. 157–163.

[18]Josyula, E., "Computational Study of Vibrationally Relaxing Gas Past Blunt Body in Hypersonic Flows," AIAA Paper 99-0866, Jan. 1999.